Research Square

Preprints are preliminary reports that have not undergone peer review.
They should not be considered conclusive, used to inform clinical practice,
or referenced by the media as validated information.

NQO1-sensitive Full-active paclitaxel nanoprodrug combining with Qi-Yu-San-Long-Decoction for efficient tumor treatment

Fan Li
Anhui University of Traditional Chinese Medicine
Haitao zheng
Anhui University of Traditional Chinese Medicine
Weisheng Xu
First Affiliated Hospital of Anhui Medical University
Annan Jiao
First Affiliated Hospital of Anhui Medical University
Fan Yang
Anhui University of Traditional Chinese Medicine
Haoyu Wu
Anhui University of Traditional Chinese Medicine
Mengmeng Yang
Anhui University of Traditional Chinese Medicine
Binqian Yao
Anhui University of Traditional Chinese Medicine
Jiabing Tong
Anhui University of Traditional Chinese Medicine
Dahai Zhao
Anhui Provincial Hospital
Nianzhi Zhang
Anhui University of Traditional Chinese Medicine
Yang Chen
First Affiliated Hospital of Anhui Medical University
Zhenbao Li
lizhenbao@ahtcm.edu.cn

Anhui University of Traditional Chinese Medicine

Research Article

Keywords: Full-active, Paclitaxel nanoprodrug, Qi-Yu-San-Long-Decoction, Chemoimmunotherapy, Non-small cell lung cancer

Posted Date: September 21st, 2026

DOI: https://doi.org/10.21203/rs.3.rs-10372842/v1

License: This work is licensed under a Creative Commons Attribution 4.0 International License.
Read Full License

Additional Declarations: No competing interests reported.

Abstract

The clinical efficacy of chemotherapy for non-small cell lung cancer (NSCLC) is often compromised by systemic toxicity, inefficient drug activation, and the inadvertent induction of an immunosuppressive tumor microenvironment *via* programmed death ligand 1 (PD-L1) upregulation. This study developed an integrative strategy combining a tumor-microenvironment-responsive nanoprodrug with the traditional Chinese medicine (TCM) formula Qi-Yu-San-Long Decoction (QYSLD) to address these limitations. A quinone oxidoreductase 1 (NQO1)-labile paclitaxel dimer prodrug was synthesized and self-assembled into “full-active” nanoparticles (PQP NPs), which exhibited uniform size, favorable stability, and rapid, NQO1-triggered drug release. *In vitro*, PQP NPs demonstrated enhanced cytotoxicity and cellular uptake. In Lewis lung carcinoma (LLC)-bearing mice, PQP NPs showed improved tumor accumulation and pharmacokinetics. When combined with QYSLD, the immunosuppressive microenvironment was synergistically reversed through the inhibition of PD-L1 expression and the regulation of macrophages and $CD4^+$/$CD8^+$ T cells. Notably, this synergism was also observed with commercially available nanomedicines. This integrative Chinese and Western medicine strategy offers a safe and efficient modality for tumor chemoimmunotherapy.

Introduction

Lung cancer is one of the leading causes of cancer-related deaths worldwide and represents a serious threat to human health [1, 2]. Currently, chemotherapy remains a crucial cornerstone for clinical lung cancer treatment, but its application faces significant challenges over the past decades [3]. As a widely used anticancer drug in clinical practice, paclitaxel (PTX) is approved as a first-line treatment regimen for lung cancer, ovarian cancer, breast cancer, and other solid tumors [4, 5]. Unfortunately, the application of PTX formulations (e.g., Taxol®, Abraxane®, and Lipusu®) is mainly constrained by the nonselective distribution, sustained drug release, dose-dependent side effects, and high toxicity resulting from systemic distribution [6]. To address these challenges, the stimuli-responsive nanoparticulated prodrug (nanoprodrug) therapeutic strategy was put forwarded [6, 7]. A prodrug is a bioreversible derivative of an active parent molecule obtained through chemical structure modification, which exhibits weak or inactive pharmacological activity *in vitro* but could transform into active drug under stimuli specific to or overexpressed in the tumor microenvironment (TME), such as reactive oxygen species (ROS), glutathione (GSH), or enzymes (e.g. Quinone Oxidoreductase 1 (NQO1), and matrix metalloproteinases (MMPs)) [6, 8, 9]. Upon integration with nanotechnology, these intelligent nanoprodrugs could passively deliver prodrug molecules into tumor tissues *via* the enhanced permeability and retention (EPR) effect and enable an on-demand drug release in the TME [8–12]. In recent years, emerging stimulus-responsive nanoprodrugs have been fabricated for efficient tumor therapy. For instance, Guo and co-researchers synthesized four acid-sensitive dextran-PTX polymeric prodrugs (named as DKPs) with different PTX-conjugating contents by ketal linker, and then utilized these DKPs to formulate DKP nanoprodrugs for antitumor therapy [10]. Through *in vitro* PTX release, cell viability, cellular uptake, and *in vivo* pharmacokinetics, biodistribution, and pharmacodynamics on 4T1-Luc and Panc02-Luc cancer models,

they reported that DKP8 nanoprodrugs exhibited faster PTX hydrolysis kinetics, superior tumor accumulation, and greater anti-tumor efficacy compared to DKP12 and DKP20 nanoprodrugs. Similarly, three hypoxia-cleavable PEGylated PTX prodrugs with azobenzene (Azo) as a responsive linker including PAP_{750}, PAP_{1K}, and PAP_{2K} were synthesized, which could self-assemble into uniform PAP NPs in aqueous solution (Sol) due to robust hydrophobic interaction [13]. Compared with insensitive PCP_{2k} NPs with ester as conjugate bond, PAP_{2k} NPs exhibited higher cytotoxicity towards HeLa cells under hypoxia milieu, and generated more effective antitumor efficacy in 4T1 breast cancer mouse models. Interestingly, additional pharmacodynamic consequences verified that PAP_{750} NPs with the shorter methoxy-PEG chain exerted a better tumor suppression activity without causing off-target toxicity. Besides, emerging stimuli-responsive nanoprodrugs such as reduction-labile PDSP nanoparticles (NPs) self-assembling by polymeric mPEG-DCA-SS-PTX conjugate (PDSP), ROS-cleavable PEG-B-PTX nanomicelles consisting of *p*-(boronic ester)benzyl-linked polyethylene glycol (PEG)-PTX conjugate were also engineered, and these nanoprodrugs exerted excellent antitumor efficiency both *in vitro* and *in vivo* [11, 12].

Despite the superior antitumor efficacy of these aforementioned NPs, these systems often exhibit limited drug loading capacity due to their high polymer molecular weight. In contrast, stimuli-cleavable small molecule self-assembly NPs could enable a facile on-demand drug activation and higher drug loading capability (over 80%) [8, 9]. In our group, various PTX-derived redox-responsive small molecule nanoprodrugs such as mono-nanoprodrugs, homodimer nanoprodrugs, and heterodimer nanoprodrugs have been successfully engineered. These nanoprodrugs exhibited robust stability, high drug loading efficiency, enhanced cytotoxicity, augmented cellular uptake, prolonged blood circulation, improved tumor distribution, and preferable antitumor effect in tumor-bearing models with minimized side effects [8, 14–18]. Apart from redox characteristics, NQO1, a two-electron oxidoreductase, is highly expressed in multiple tumor cells, making it a potential trigger for enzyme-activated drug release [19]. Several NQO1-responsive nanoprodrugs such as DQP NPs consisting of quinone dipropionic acid (QDPA)-conjugated dimer PTX prodrug, DQMe NPs composed of QDPA-linked fluorescence quenched Me (QMe), CM-ICG@IrQ derived from hydrophilic drug Irinotecan and phototherapy agent ICG, and PDox@origami constructed by quinone propionic acid-Dox prodrug (PDox) and DNA origami have been developed for promising tumor theranostics [20, 21]. Similar to these reports, we have successfully fabricated NQO1-responsive dimer PTX nanoprodrug, PQP NPs, and found that PQP NPs were capable of triggering strong immunogenic cell death (ICD) and activating T cells to initiate an adaptive immune response. However, in line with our previous small molecule prodrug self-assemblies, PQP NPs also induced the upregulation of PD-L1 expression in tumor cells, thereby suppressing T-cell function and aggravating the formation of immunosuppressive microenvironment to confront the chemotherapeutic capacity and ICD effect of PTX.

Traditional Chinese medicine (TCM) represents a precious cultural heritage of the Chinese nation due to its efficient therapeutic potential, millennia-old history, substantial clinical experience, holistic treatment perspective and personalized medical regimen, which have gained recognition and popularity in the

world, and attracted increasing attention for superior therapeutic activity in disease prevention and management [22–24]. Qi-Yu-San-Long-Decoction (QYSLD) is a well-known traditional medicine for the treatment of NSCLC in clinical practice and is composed of Astragalus membranaceus, Polygonatum odoratum, Tianlong, Dilong, Solanum nigrum, Hedyotis diffusa, Coix seed, Euphorbia helioscopia, Curcuma zedoaria, and Fritillaria cirrhosa [25]. Previous clinical studies have demonstrated that QYSLD can not only stabilize tumors and improve patients' quality of life, but also exert antitumor activity through the regulation of the PI3K/Akt/mTOR and Wnt/β-catenin signaling pathways [25]. More importantly, QYSLD can significantly down-regulate the mRNA and protein levels of PD-L1 in tumor tissues, remodel the tumor immune microenvironment, inhibit tumor cell immune escape, and enhance antitumor immune response [25]. This finding provides a crucial basis for the synergistic immunotherapy of PTX nanoprodrug combining with QYSLD [9, 25].

From the TCM pathogenesis of lung cancer, persistent deficiency of healthy qi and yin impairs host defense, while phlegm turbidity, blood stasis, and toxic accumulation gradually form pulmonary masses. Under the monarch-minister-assistant-courier principle, QYSLD can be interpreted as a structured formula rather than a simple herbal mixture. Astragalus membranaceus and Polygonatum odoratum serve as monarch herbs to reinforce qi, nourish yin, and protect the host defense system. Solanum nigrum, Hedyotis diffusa, Euphorbia helioscopia, and Curcuma zedoaria act as minister herbs to clear heat and toxin, activate blood, resolve stasis, and directly target tumor-associated pathogenic factors. Tianlong and Dilong function as assistant herbs to unblock collaterals, disperse masses, and enhance the penetration of the anti-tumor action into the tumor microenvironment. Coix seed and Fritillaria cirrhosa further assist and guide the prescription by strengthening the spleen, resolving dampness and phlegm, and directing the therapeutic effect toward the lung. This compatibility logic provides a theoretical basis for combining QYSLD with PTX nanoprodrugs: the formula regulates the systemic and immune microenvironment, whereas the nanoprodrug provides precise cytotoxic elimination of tumor cells.

Herein, full-active dimer PTX nanoprodrug PQP NPs were successfully engineered using the one-step nanoprecipitation method, which could self-assemble into uniform NPs with high stability, maintain a prolonged blood circulation after intravenous injection, and then passively accumulate in tumor tissues *via* the EPR effect. In comparison with insensitive PCP group self-assembling by carbon-linked PTX-C-PTX NPs, the highly expressed NQO1 enzyme of the TME specifically activated PQP NPs, and triggered QDPA cleavage and rapid release of PTX to induce efficient ICD effect and chemotherapeutic outcome. Meanwhile, the intragastric administration of QYSLD could synergistically remodel the TME, down-regulate the expression of PD-L1, and reverse the immunosuppressive state, thereby generating an enhanced chemoimmunotherapeutic outcome in Lewis lung carcinoma (LLC)-bearing mice. Furthermore, QYSLD also demonstrated synergistic antitumor and immunomodulatory effects when combined with commercially available nanomedicines, underscoring the broad applicability of this integrated strategy. This combinational therapy perspective by the integration of TCM and western nanoparticulated delivery provides an innovative insight for the efficient treatment of lung cancer. In this integrated design, PQP NPs were positioned as the modern pharmacological component for “eliminating

pathogenic tumor toxin” through NQO1-responsive PTX release and ICD induction, while QYSLD was positioned as the TCM regulatory component for “supporting healthy qi and correcting the tumor immune terrain” through PD-L1 downregulation and immune-cell remodeling (Scheme 1).

Materials and methods

Cells and animals

LLC, human non-small cell lung cancer (A549), and mouse fibroblast (L929) cells were obtained from the Experimental Center of Anhui Medical University.

C57BL/6J mice (18–22 g) and male Sprague-Dawley (SD) rats (200–220 g) were purchased from Henan Skobes Biotechnology Co., Ltd. Animal experiments were performed in accordance with the "Laboratory Animal Management Regulations" and approved by the Animal Ethics Committee of Anhui University of Traditional Chinese Medicine. Ethical batch number: AHUCM-mouse-2024151, AHUCM-rats-2024149.

Materials

The herbal components of QYSLD were obtained from the First Affiliated Hospital of Anhui University of Traditional Chinese Medicine and were authenticated by the Department of Pharmacy. The batch numbers of the herbs were as follows: Astragalus membranaceus (2304140041), Polygonatum odoratum (2309250222), Tianlong (2304280022), Dilong (2303190122), Longkui (2302270312), Baihuasheshecao (2310190042), Yiyiren (2308080252), Zeqi (2308230292), Ezhu (2302270092), and Chuanbeimu (2309260312). All herbs were supplied by Bozhou Huqiao Pharmaceutical Co., Ltd. in line with the provisions of the “Chinese Pharmacopoeia”.

According to the Jun-Chen-Zuo-Shi compatibility framework, the herbs of QYSLD were categorized functionally as follows: Astragalus membranaceus and Polygonatum odoratum as monarch herbs for qi-yin reinforcement; Solanum nigrum, Hedyotis diffusa, Euphorbia helioscopia, and Curcuma zedoaria as minister herbs for heat-toxin clearance, blood activation, and mass resolution; Tianlong, Dilong, and Coix seed as assistant herbs for collateral-unblocking, dampness resolution, and reinforcement of anti-tumor penetration; and Fritillaria cirrhosa as an assistant/courier herb for phlegm resolution and lung-oriented guidance. This theoretical categorization was used to interpret the biological cooperation between QYSLD and PTX-based nanomedicine in subsequent experiments.

All chemicals were commercially available and used without further purification. Coumarin-6 (C6) (B2088-1G) and Enhanced Cell Counting Kit-8 (CCK-8) (C0041) were obtained from Beyotime Biotechnology Co., Ltd. (Shanghai, China); 1,1-dioctadecyl-3,3,3,3-tetramethylindotricarbocyanine iodide (DiR) (MB12482-2) was bought from Dalian Meilun Biotechnology Co., Ltd. (Dalian, China); Anti-CD4-FITC (100526), Anti-CD8-APC (100734), Anti-CD80-PE (104714), and Anti-CD206-APC (141706) were purchased from BioLegend Biotechnology Co., Ltd. (Shanghai, China); Anti-PD-L1 (AB213480) and Anti-GAPDH (AB181602) were bought from Abbott Trading Co., Ltd. (Shanghai, China); Horseradish

peroxidase-labeled goat anti-rabbit IgG (Z952240826) was obtained from Beyotime Biotechnology Co., Ltd. (Shanghai, China).

The following instruments were used in this study: High Performance Liquid Chromatography (HPLC) (UltiMate 3000, Agilent Technologies, Shanghai, China), Multi-function Microplate Reader (SpectraMax i3X, Molecular Devices, USA), Flow Cytometer (FCM) (BD FACSCelesta, BD, USA), Confocal Laser Scanning Microscopy (CLSM) (Operetta CLS, PerkinElmer, USA), Chemiluminescence Imager (Tanon 5200, Shanghai Tianneng Technology Co., Ltd., China), Malvern Zetasizer (ZEN3690, Malvern Panalytical Inc., Westborough, MA, USA), and Transmission Electron Microscopy (TEM) (JEOL-2010, Hitachi, Japan).

Synthesis of PTX-Q-PTX

Synthesis of 2,5-dimethyl-hydroquinone

2,5-Dimethylhydroquinone was prepared by reducing 2,5-dimethyl-p-benzoquinone with sodium dithionite in a biphasic system of ether and water under a nitrogen atmosphere. After stirring for 4 h, the product was isolated by standard workup including extraction, washing with brine, and drying (Na_2SO_4). Subsequent solvent removal afforded the product as a light-yellow solid in high yield and purity.

Synthesis of dilactone chromanone derivatives

dilactone chromanone derivatives were synthesized in a one-pot condensation of 2,5-dimethylhydroquinone and 3,3-dimethyl acrylate, employing methanesulfonic acid as both solvent and catalyst at 70°C. Following a 48 h reaction period, the product was isolated by extraction into ethyl acetate, washed, concentrated, and obtained as a white solid upon precipitation.

Synthesis of QDPA

QDPA was obtained as a yellow solid following lithium hydroxide-mediated hydrolysis of the corresponding dilactone in THF/water. After stirring for 1 h at room temperature, the reaction mixture was acidified to pH 3 – 4 with dilute HCl, and the product was isolated by extraction into ethyl acetate, followed by concentration under reduced pressure.

Synthesis of PQP

The dimeric prodrug PTX-Q-PTX was synthesized by coupling PTX with QDPA using EDCI/DMAP as coupling catalysts in a two-stage addition manner under nitrogen. After a total reaction time of 24 h, the product was isolated via preparative liquid chromatography.

Synthesis of PCP

The non-responsive dimer PTX prodrug PCP was synthesized by coupling PTX with sebacic acid using EDCI/DMAP in a two-stage addition process. The crude product was concentrated and purified via preparative liquid chromatography to obtain the final compound.

The purity of PQP and PCP was analyzed by HPLC under the following conditions: detection wavelength of 227 nm, isocratic elution with a mobile phase of acetonitrile/water (70:30, *v*/*v*), and column temperature maintained at 30°C.

Characterization of full-active NPs

Full-active self-assembling NPs, exemplified by PQP NPs, were prepared using a one-step nanoprecipitation method. Briefly, 4 mg of PQP and 8 mg of 1,2-distearoyl-sn-glycero-3-phosphoethanolamine-polyethylene glycol 2000 (DSPE-PEG_{2K}) in a mixed organic solvent were injected into deionized water. After stirring for 1 h and removing organic solvents, the NPs were obtained. The resulting NPs were characterized for size and zeta potential by dynamic light scattering (DLS), and morphology by TEM after negative staining.

Stability of full-active NPs

PQP NPs and PCP NPs were incubated in PBS (pH 7.4) containing 10% fetal bovine serum in a thermostatic oscillator (100 rpm) at 37°C. The particle size of NPs was measured at 0, 2, 4, 6, 8, 10, 12, 24, and 48 h. Additionally, the long-term storage stability of these full-active NPs was evaluated at 4°C.

drug release

In vitro drug release
The *in vitro* release of PTX was quantified by HPLC. Release media were prepared by dissolving $Na_2S_2O_4$ in PBS (pH 7.4) containing 30% anhydrous ethanol to achieve $Na_2S_2O_4$ concentrations of 30 mM and 60 mM. An appropriate amount of PQP NPs was added to each release medium, and the mixtures were incubated in a thermostatic shaker (37°C, 100 rpm). At each predetermined time point (0, 0.5, 1, 3, 6, 9, 12, 24, 36, and 48 h), 100 μL of sample was collected, and the concentration of PTX was quantified by HPLC (detection wavelength of 227 nm). Additionally, the morphology of PQP NPs was examined after incubation with the $Na_2S_2O_4$ release media using TEM. The release characteristics and morphology of PCP NPs were also assessed.

Preparation of QYSLD powder

A mixture of 30 g Astragalus, 20 g Solanum nigrum, 20 g Hedyotis diffusa, 20 g Coix seed, 10 g Polygonati Odorati Rhizoma, 10 g Zedoary Rhizome, 10 g Gecko, 6 g Earthworm, and 6 g Euphorbia helioscopia was soaked with 10 volumes of distilled water for 1 h, and then decocted over a fire for 90

min. The mixture was filtered to obtain filtrate and residue, and then the collected residue underwent second decoction for another 40 min. Finally, the filtrate was combined and concentrated by rotary evaporator at 50°C to a concentration of 2 g/mL to obtain QYSLD extract. The extract was freeze-dried to prepare QYSLD powder, which was stored at − 20°C for subsequent experiments. The decoction procedure preserved the traditional water-extraction characteristics of the prescription and was intended to maintain the multi-component compatibility of monarch, minister, assistant, and courier herbs, thereby supporting the interpretation of QYSLD as a holistic immunomodulatory adjuvant rather than a single-target cytotoxic agent.

Cell viability and uptake

LLC, A549, and L929 cells were cultured in DMEM supplemented with 10% (*v*/*v*) heat-inactivated FBS (Gibco). The cells were maintained in a humidified incubator with 5% CO_2 at 37°C, and the culture medium was refreshed daily. The cytotoxicity of Taxol, PQP NPs, PCP NPs, QYSLD, PQP NPs&QYSLD, and PCP NPs&QYSLD was evaluated in LLC, A549, and L929 cells *via* the CCK-8 assay. Briefly, the cells were seeded in 96-well plates and incubated with the respective treatment groups for 48 h. Then, CCK-8 Sol was added, and the optical density (OD) was measured at 450 nm using a microplate reader.

The cellular uptake of C6-labeled NPs was assessed using qualitative CLSM and quantitative FCM. C6-Sol and C6-labeled NPs were prepared according to the previous method[9]. LLC, A549, and L929 cells were cultured in 6-well plates for 24 h, then treated with C6-Sol or C6-labeled NPs (200 or 500 ng/mL C6 equivalent) for 0.5 h and 2 h. After incubation, the cells were divided for analysis: one portion was washed, fixed, and stained with DAPI for CLSM imaging, while the other portion was trypsinized, washed, and resuspended for FCM analysis.

Pharmacokinetics

Male SD rats (180–220 g) were randomly divided into five groups (*n* = 3). To evaluate the pharmacokinetics, PQP NPs and PCP NPs were labeled with DiR to obtain PQP NPs/DiR and PCP NPs/DiR, respectively. Free DiR and DiR-labeled NPs were injected into the tail vein at a DiR dose of 2 mg/kg. Meanwhile, QYSLD (80.48 g/kg, equivalent to 4 times the clinical adult dosage) was orally administered to the PQP NPs/DiR&QYSLD and PCP NPs/DiR&QYSLD groups. Blood samples were collected from the ophthalmic vein plexus of SD rats at predetermined time points (0.083, 0.25, 0.5, 1, 2, 4, 8, 12, and 24 h). The samples were placed in Eppendorf tubes coated with heparin sodium and centrifuged (8,000 rpm, 3 min) to isolate plasma. Next, 50 μL of the supernatant (plasma) was mixed with 450 μL of methanol, vortexed thoroughly, centrifuged (12,000 rpm, 10 min), and the resulting supernatant was transferred to a 96-well plate for fluorescence intensity measurement using a multifunctional microplate reader (λ□□ = 748 nm, λ□□ = 780 nm).

Biodistribution

An LLC tumor-bearing model was established by subcutaneous injection of LLC cells (2×10^6) into the right flank of male C57BL/6J mice. When the tumor volume reached approximately 300 mm^3, DiR-Sol, PQP NPs/DiR, and PCP NPs/DiR groups were intravenously injected at an equal DiR dose of 2 mg/kg. Concurrently, the PQP NPs/DiR&QYSLD and PCP NPs/DiR&QYSLD groups received an additional 80.48 g/kg of QYSLD by oral gavage. At 4 h and 24 h post-injection, three mice in each group were sacrificed, and whole-body fluorescence imaging was performed using an *in vivo* imaging system (λ_{ex} = 748 nm, λ_{em} = 780 nm). Subsequently, the isolated heart, liver, spleen, lungs, kidneys, and tumor from each mouse were also imaged to quantify the fluorescence distribution of DiR-labeled NPs.

Pharmacodynamics and safety of QYSLD in combination with full-active NPs

An LLC tumor-bearing model was established in male C57BL/6J mice (20–25 g). When the tumor volume reached 100–150 mm^3, the mice were randomly assigned into seven groups (n = 5): Saline, Taxol, QYSLD, PQP NPs, PQP NPs&QYSLD, PCP NPs, and PCP NPs&QYSLD. The equivalent dose of PTX was 10 mg/kg *via* tail vein injection, and the dose of QYSLD was 80.48 g/kg by oral gavage. During the treatment period, the body weight and tumor volume of the mice were measured daily. On day 15, the mice were sacrificed, and the hepatorenal function and hematological parameters were analyzed to evaluate the safety of the intravenously administered NPs. Major organs (heart, liver, spleen, lungs, and kidneys) and tumors were collected, fixed in 4% paraformaldehyde, and stained with hematoxylin and eosin (H&E) to assess the potential toxicity in the major organs and the degree of cancer cell apoptosis. Additionally, tumor proteins were extracted from homogenized tissues and analyzed by Western blotting. For immune cell assessment, cell suspensions from tumors were prepared, stained with specific fluorescent antibodies against CD4, CD8, CD80, and CD206, and quantified by FCM.

Pharmacodynamics and safety of QYSLD in combination with commercially available nanomedicines

An LLC tumor-bearing model was established in male C57BL/6J mice (20–25 g). Upon reaching tumor volumes of 100–150 mm^3, mice were randomized into nine groups (n = 5): Saline, QYSLD, double dose QYSLD (2QYSLD), Lipusu, Abraxane, Lipusu&QYSLD, Lipusu&2QYSLD, Abraxane&QYSLD, and Abraxane&2QYSLD. The equivalent dose of PTX was 10 mg/kg *via* tail vein injection, and the dose of QYSLD was 80.48 g/kg by oral gavage. Body weight and tumor volume were monitored daily. On day 17, mice were euthanized, and tumors were excised and weighed to assess therapeutic efficacy.

Results and discussion

Preparation, characterization and release of full-active NPs

The synthesis of PQP was carried out as shown in **Figure S1**, and the chemical structures of 2,5-dimethyl-hydroquinone, dilactone chromanone derivatives, QDPA, and PQP were confirmed by nuclear magnetic resonance spectroscopy (^{1}H-NMR) and high-resolution mass spectrometry (HR-MS) (**Figure**

S2-S5). The synthesis of PCP was achieved by the esterification of PTX and sebacic acid (**Figure S6**) and the structure was also characterized by ^{1}H-NMR and HR-MS (**Figure S7**). The purity of PQP and PCP was determined by HPLC. The results indicated that both PQP and PCP possessed a purity exceeding 96%, which met the requirements for nanoprodrug formulation.

Similar to the facile self-assembly of PTX-derived prodrugs in our previous reports, PQP NPs and PCP NPs were prepared *via* a one-step nanoprecipitation method using DSPE-PEG_{2k} as a stabilizer [6, 8, 9]. As presented in Fig. 1A and B, PQP NPs and PCP NPs exhibited a uniform spherical morphology with average hydrodynamic diameters of approximately 103 nm and 115 nm, respectively. The polydispersity index (PDI) was within an appropriate range (PQP NPs: 0.18 ± 0.04, PCP NPs: 0.09 ± 0.04), confirming the good monodispersity of the NPs. The zeta potentials of PQP NPs and PCP NPs were − 43.50 and − 42.60 mV, respectively (Fig. 1C). The negative surface charge and small particle size contribute to prolonged circulation time and enhanced tumor accumulation upon intravenous administration[29]. The colloidal stability of the NPs was evaluated by incubating PQP NPs and PCP NPs in PBS (pH 7.4) containing 10% FBS for 48 h, and the long-term storage stability was assessed at 4°C for 21 days. The changes in hydrodynamic diameter were monitored by DLS. As illustrated in Fig. 1D and E, the particle sizes of PQP NPs and PCP NPs remained largely unchanged both in PBS containing 10% FBS and during storage at 4°C, indicating excellent stability. To elucidate the assembly mechanism of NPs, the influence of Water, NaCl, Urea, and sodium dodecyl sulfate (SDS) on particle size was examined. As demonstrated in Fig. 1F and G, the presence of SDS remarkably increased the particle size and PDI of both PQP NPs and PCP NPs, confirming that hydrophobic interactions are the primary driving force for the formation and stability of these nanostructures. Molecular docking simulations were performed to calculate the free energy of prodrug self-assembly and further assess the stability and self-assembly capability. Thermodynamic analysis (Fig. 1H and I) revealed that the free energy of assembly for PQP and PCP was − 7.1 kcal/mol and − 6.1 kcal/mol, respectively. These findings demonstrated that the QDPA linker endows PQP NPs with a lower free energy, higher self-assembly activity, and a smaller particle size compared to PCP NPs, which may underlie its favorable *in vivo* performance.

To evaluate the NQO1-responsiveness of NPs, PQP NPs and PCP NPs were incubated in media containing varying concentrations of $Na_2S_2O_4$ (30 mM and 60 mM) to mimic the NQO1-overexpressing TME. The PTX release was then quantified by HPLC. As shown in Fig. 1J, the PTX release profiles revealed that PQP NPs exhibited a concentration-dependent response to $Na_2S_2O_4$, achieving approximately 80% PTX release with 30 mM $Na_2S_2O_4$ and nearly complete release (~ 100%) with 60 mM $Na_2S_2O_4$ within 48 h. In contrast, PCP NPs showed negligible PTX release under identical conditions, verifying the crucial role of the QDPA linkage in NQO1-induced PTX release. The release mechanism involves an NQO1-triggered nucleophilic attack by hydroxyl groups on the carbonyl moiety, leading to rapid lactone formation, cleavage of the ester bond, and thereby facilitating PTX release from PQP NPs (Fig. 1K). After incubation with 60 mM $Na_2S_2O_4$ for 12 h, TEM images showed that PQP NPs were substantially disintegrated, whereas PCP NPs retained their intact nanostructure (Fig. 1L). These results

demonstrate that PQP NPs exhibit strong NQO1-mediated sensitivity and enable on-demand PTX release in the TME.

In vitro anti-tumor efficiency

To investigate the combinatorial anti-tumor effect of QYSLD and NPs, we first performed the CCK-8 assay to evaluate the cytotoxicity of each formulation against tumor (LLC, A549) and normal (L929) cells. The results in Fig. 2A-C revealed that QYSLD and PTX prodrug NPs presented a concentration-dependent anti-tumor activity. In comparison with normal L929 cells (IC_{50}: 28.11 μM), PQP NPs displayed higher cytotoxicity against LLC (IC_{50}: 3.84 μM) and A549 cells (IC_{50}: 3.75 μM). Notably, PQP NPs demonstrated superior cytotoxicity against tumor cells compared to PCP NPs (Table 1). This selective toxicity is attributed to the high expression of the NQO1 enzyme in tumor cells, which could facilitate the cleavage of PQP NPs and release PTX into the cytoplasm, whereas PTX release from PQP NPs in L929 cells was limited due to low NQO1 expression. When combined with QYSLD, the PQP NPs&QYSLD and PCP NPs&QYSLD groups exhibited higher cytotoxicity than the corresponding NPs or QYSLD alone, demonstrating a synergistic therapeutic effect between the TCM and chemotherapeutic PTX. From the perspective of “supporting healthy qi and eliminating pathogens”, the enhanced cytotoxicity of PQP NPs&QYSLD suggests that QYSLD does not simply duplicate the cytotoxic role of PTX, but complements PTX-based tumor killing by modifying the cellular and immune regulatory context in which chemotherapy acts.

Next, we explored the cellular uptake of C6-labeled NPs in LLC, A549, and L929 cells. The combination groups were treated with NPs (C6 equivalent concentration: 200 ng/mL) in complete medium containing QYSLD at its respective IC_{50} values (LLC: 15.02 mg/L, A549: 18.65 mg/L, and L929: 18.16 mg/L). CLSM observation revealed time-dependent cellular uptake of PQP NPs/C6 and PCP NPs/C6 in LLC, A549, and L929 cells (Fig. 2D-F), whose uptake efficiency were significantly higher than that of C6-Sol. This difference in cellular internalization may result from distinct mechanisms: NPs was internalized mainly *via* energy-dependent endocytosis, whereas free hydrophobic molecules enter cells through passive diffusion. Importantly, the addition of QYSLD exerted a negligible influence on NPs uptake, suggesting the excellent stability of NPs and distinct cellular uptake pathways. Additionally, the corresponding quantification of intracellular fluorescence by FCM depicted a consistent result with the aforementioned consequence by CLSM (Fig. 2G-I).

Recent studies have documented that PD-L1 is commonly overexpressed on the membrane of numerous malignancies, which is significantly associated with poor prognosis in patients [26–28]. More importantly, tumor-associated fibroblasts, lymphocytes, and macrophages in the tumor microenvironment often help tumor cells escape immune surveillance and impair therapeutic outcomes. Blockade of the PD-1/PD-L1 pathway between tumor cells and T cells could effectively reverse immunosuppression and reactivate T cell activity against tumor cells. Currently, PD-1/PD-L1 blockade approved in clinic are monoclonal antibodies such as Keytruda, OPDIVO, atezolizumab, and durvalumab. However, their therapeutic efficacy is limited by the poor immune response, primary or acquired

resistance, and exorbitant price for cancer patients [29]. Previous studies from our group have demonstrated the antitumor activity of QYSLD and its ability to enhance therapeutic efficacy. In our affiliated hospital (The First Affiliated Hospital of Anhui University of Chinese Medicine), QYSLD has been widely used in the clinical treatment of lung cancer [9]. To investigate whether QYSLD could enhance the therapeutic efficacy of PQP NPs and PCP NPs, we examined the influence of QYSLD on PD-L1 expression in tumor cells in combination with the NPs using FCM and Western blotting. As shown in Fig. 2J-L, QYSLD downregulated PD-L1 expression on tumor cells compared to the untreated group. In contrast, treatment with Taxol, PQP NPs, and PCP NPs markedly upregulated the PD-L1 expression. However, when combined with QYSLD, PQP NPs&QYSLD and PCP NPs&QYSLD exhibited significantly reduced PD-L1 levels. This observation was further corroborated by Western blot analysis (**Figure S9A** and **B**) in LLC cells, collectively confirming the regulatory effect of QYSLD.

In TCM terms, chemotherapy-induced PD-L1 upregulation may be regarded as a modern biological manifestation of unresolved pathogenic factors and impaired healthy qi after tumor attack. The ability of QYSLD to suppress PD-L1 expression is therefore consistent with its monarch-minister-assistant-courier compatibility: monarch herbs support host defense, minister herbs clear toxin and resolve tumor-associated pathogenic factors, and assistant/courier herbs improve microenvironmental communication by resolving phlegm, activating blood, and unblocking collaterals. This provides a theoretical explanation for why QYSLD can transform PTX-induced ICD from a potentially restrained immune response into a more effective chemoimmunotherapeutic process.

Pharmacokinetics and biodistribution

To investigate the pharmacokinetics and biodistribution, PQP NPs and PCP NPs were labeled with DiR to obtain PQP NPs/DiR and PCP NPs/DiR. For the pharmacokinetic study, SD rats were intravenously injected with the DiR-labeled NPs at a dose of 2 mg DiR/kg. Simultaneously, 80.48 g/kg QYSLD was administrated by oral gavage to determine whether it could result in a differentiated pharmacokinetic impact on these intravenously injected NPs. At predetermined time points, blood was collected, processed with methanol for extraction, and the interior fluorescence intensity was measured by microplate reader (Fig. 3A). As depicted in Fig. 3B and Table 2, DiR-labeled NPs exhibited a larger area under the plasma concentration curve (AUC_{0-24h}) than DiR-Sol, indicating that the NPs could prolong the blood circulation time of DiR due to the protection of hydrophilic PEG corona on the NPs surface. Similar to the *in vitro* cellular uptake results, we found that the oral QYSLD had no significant effect on the blood circulation of the NPs. The absence of a marked pharmacokinetic interference by QYSLD supports the rationality of this integrated regimen: QYSLD mainly contributes systemic immune and microenvironmental regulation, while the PEGylated nanoprodrug independently maintains prolonged circulation and tumor accumulation.

Next, we established an LLC tumor-bearing model in C57BL/6J mice and used DiR-labeled NPs to investigate their biodistribution. In line with the pharmacokinetic dosage regime, DiR-Sol, PQP NPs/DiR, and PCP NPs/DiR groups were intravenously injected at a DiR dosage of 2 mg/kg, and 80.48 g/kg QYSLD

was orally administered by gavage concurrently for the PQP NPs/DiR&QYSLD and PCP NPs/DiR&QYSLD groups. Fluorescence signals were monitored at 4 and 24 h after intravenous injection using an *in vivo* fluorescence imaging system. As shown in Fig. 3C, DiR-Sol primarily accumulated in the liver and lungs, with negligible distribution in tumor tissue. In contrast, PQP NPs/DiR, PCP NPs/DiR, PQP NPs/DiR&QYSLD and PCP NPs/DiR&QYSLD exhibited higher fluorescence intensity in tumor than DiR-Sol. Furthermore, the NIR imaging of excised major organs and tumor tissues confirmed that the NPs achieved efficient tumor accumulation, attributable to the prolonged blood circulation and the passive EPR effect (Fig. 3D and E). Additionally, both the *in vivo* fluorescence accumulation and the *in vitro* NIR imaging of resected tissues demonstrated that QYSLD did not significantly alter the biodistribution of the NPs.

In vivo antitumor efficacy and safety

Encouraged by the preferable blood circulation and tumor accumulation, we established an LLC tumor-bearing mouse model to evaluate the therapeutic efficacy and safety of the NPs in combination with QYSLD. As illustrated in Fig. 4A, LLC cells (2×10^6 cells/mouse) were subcutaneously implanted into the right flank of C57BL/6J mice. When tumor volumes reached approximately 150 mm^3, the mice were randomly divided into seven groups: Saline, Taxol, PQP NPs, PCP NPs, QYSLD, PQP NPs&QYSLD, and PCP NPs&QYSLD. The NPs were administered intravenously at a PTX dose of 10 mg/kg, and QYSLD was orally administered at 80.48 g/kg. Tumor volumes and body weights were measured daily. After 15 days of treatment, mice were sacrificed and tumor tissues were collected. As shown in Fig. 4B, compared with the Saline group, the PCP NPs, QYSLD, and PCP NPs&QYSLD groups exhibited moderate antitumor efficacy, while the PQP NPs and PQP NPs&QYSLD demonstrated a more effective tumor growth inhibition, with a comparable antitumor efficiency to Taxol. Furthermore, photographs of excised tumors and tumor weight measurements (Fig. 4C and D) confirmed the superior tumor suppression effect, consistent with the *in vitro* cytotoxicity results. Additionally, as indicated in Fig. 4F, the representative H&E and TUNEL staining confirmed that both Taxol and PQP NPs&QYSLD could induce distinct tumor cell necrosis and apoptosis, demonstrating the superior antitumor efficacy of the QYSLD and PQP NPs combination. This treatment design reflects a division of therapeutic roles: PQP NPs provide targeted elimination of tumor burden, whereas QYSLD provides formula-level regulation of the host-tumor balance, corresponding to the TCM concept that anti-cancer therapy should avoid “attacking the pathogen without supporting the healthy qi”.

The biosafety of the treatment groups was evaluated based on body weight changes, liver and kidney function, hematological parameters, and H&E staining of major organs. Compared with the initial body weights of tumor-bearing mice, no significant body weight loss was observed in treated groups with the exception of the Taxol group (**Figure S10**), indicating that Taxol exhibited considerable systemic toxicity due to its non-selective biodistribution after intravenous administration. Moreover, H&E staining of major organs revealed no obvious histological damage in the treatment groups (**Figure S11A**) suggesting that NPs and conditional groups caused little organ toxicity. In addition, there was no significant difference in

blood routine, liver function, or kidney function of mice in different treatment groups (**Figure S11B** and **C**), which further confirmed their favorable hematological and biochemical safety profiles. The above results proved that the combination of QYSLD and the NPs exhibited good safety.

Next, we investigated PD-L1 expression in tumor tissues by Western blot. As shown in Fig. 4E, compared with the Saline group, the PQP NPs, PCP NPs, and Taxol significantly upregulated PD-L1 expression. The PQP NPs group showed the highest PD-L1 level, which can be attributed to the efficient tumor accumulation and rapid NQO1-triggered PTX release. Notably, QYSLD effectively downregulated PD-L1 expression when combined with the NPs (PQP NPs&QYSLD, PCP NPs&QYSLD). Moreover, we utilized FCM to analyze the changes in the proportions of $CD4^+$ T cells, $CD8^+$ T cells, M1 and M2 macrophages in tumor tissue following treatment. As illustrated in Fig. 5, in contrast with single NPs treatment, the combination therapy groups substantially increased the proportion of $CD4^+$ T and $CD8^+$ T cells within tumor tissues. Meanwhile, analysis of tumor-associated macrophages (TAMs) revealed that QYSLD and the combination groups significantly reduced the proportion of immunosuppressive M2 macrophages while increasing that of immunostimulatory M1 macrophages, indicating that QYSLD promotes TAM repolarization from the M2 to the M1 phenotype. In conclusion, the results presented that QYSLD could downregulate PD-L1 expression in tumor cells and remodeled the immunosuppressive microenvironment by increasing the proliferation of of $CD4^+$ T cells, $CD8^+$ T cells, and M1 macrophages while decreasing M2 macrophages, thereby synergistically enhancing the antitumor efficacy in combination with the chemotherapeutic NPs. These immunological findings translate the Jun-Chen-Zuo-Shi theory into measurable biological outcomes: qi-yin reinforcement corresponded to improved T-cell infiltration, toxin clearance and stasis resolution corresponded to reduced PD-L1-associated immune escape, and phlegm-stasis dispersal/collateral unblocking corresponded to macrophage repolarization from the M2 phenotype toward the M1 phenotype. Thus, QYSLD converted the immune-suppressive “phlegm-stasis-toxin” microenvironment into an immune-activated state that was more receptive to PTX nanoprodrug-induced ICD.

Finally, we assessed the *in vitro* anti-tumor efficacy of QYSLD in combination with commercially available nanomedicines (Lipusu, Abraxane) in LLC tumor-bearing mice. The experimental protocol is illustrated in Fig. 6A. When the tumor volume reached approximately 150 mm^3, the mice were randomly assigned to nine groups: Saline, QYSLD, 2QYSLD, Lipusu, Abraxane, Lipusu&QYSLD, Lipusu&2QYSLD, Abraxane&QYSLD, and Abraxane&2QYSLD. As depicted in Fig. 6B, the tumor volume in the Saline group increased rapidly, whereas the treatment of QYSLD, 2QYSLD, Lipusu, and Abraxane partially inhibited tumor growth. Notably, the Lipusu&2QYSLD and Abraxane&2QYSLD groups demonstrated greater efficacy in tumor suppression compared to Abraxane or Lipusu alone. Representative tumor photographs and weights confirmed the above results (Fig. 6C and D). H&E and TUNEL staining results indicated that Abraxane&2QYSLD had significant necrosis and apoptosis (Fig. 6F). We further investigated the biosafety of all treatment groups. The body weight of mice in all groups fluctuated within the normal range during the treatment (Fig. 6E). H&E staining of the heart, liver, spleen, lungs, and kidneys from all groups demonstrated no obvious histological damage (**Figure S12A**). Compared to the

Saline group, the other treatment groups exhibited no significant alterations in blood routine parameters, liver function, or kidney function (**Figure S12A** and **B**). FCM was performed to detect the expression of $CD4^+$ T cells, $CD8^+$ T cells, M1 and M2 macrophages in the tumor tissues. The results exhibited an increased proportion of $CD4^+$ T cells and $CD8^+$ T cells (Fig. 7A, C, and D), a reduced proportion of M2 macrophages, and an increased proportion of M1 macrophages (Fig. 7B, E, and F) in the Abraxane&2QYSLD group. In summary, our results confirm a synergistic anti-tumor effect between QYSLD and commercially available nanomedicines, characterized by induced tumor cell death and a favorable immunomodulatory response. The efficacy of QYSLD combined with Lipusu or Abraxane further indicates that the TCM component is not restricted to a single nanoprodrug structure; rather, its Jun-Chen-Zuo-Shi-based immune and microenvironmental regulation may serve as a broadly applicable adjuvant principle for PTX-centered chemoimmunotherapy.

Conclusion

Herein, we synthesized an NQO1-sensitive PTX dimer prodrug (PQP) using QDPA as a cleavable linker and subsequently prepared full-active PQP NPs *via* a one-step nanoprecipitation method. The resulting NPs demonstrated excellent colloidal stability, NQO1-responsive PTX release, potent cytotoxicity, prolonged blood circulation, and enhanced tumor accumulation following intravenous administration. When combined with QYSLD, the PQP NPs& QYSLD exhibited optimal antitumor efficacy with minimal side effects. This synergistic effect can be attributed to the effective chemotherapy from NQO1-triggered PTX release coupled with the immunomodulatory effects of QYSLD, which include enhanced $CD4^+/CD8^+$ T-cell infiltration, promoted repolarization of M2 to M1 macrophages, and downregulated PD-L1 expression in tumors. Importantly, the combination of QYSLD with commercially available nanomedicines also exhibited enhanced antitumor activity and immune remodeling, underscoring the translational potential of this integrated approach. This study offers an innovative therapy paradigm for NSCLC by combining TCM with NPs, and pave a promising for chemotherapeutic translations. From the TCM theoretical viewpoint, QYSLD follows the Jun-Chen-Zuo-Shi compatibility principle and provides a coordinated strategy of reinforcing qi and nourishing yin, clearing toxin, resolving phlegm, activating blood, dispersing masses, and unblocking collaterals. The combination with PQP NPs therefore represents a bidirectional integrated therapy in which the nanoprodrug precisely attacks tumor cells and induces ICD, while QYSLD restores anti-tumor immune surveillance and prevents chemotherapy-associated immune escape. This theoretical-biological coherence strengthens the rationale for integrating QYSLD with PTX-based nanomedicine in NSCLC chemoimmunotherapy.

Declarations

Ethics approval

Animal experiments were performed while respecting the ethics and regulation of animal experimentation (Approval Nos. AHUCM-mouse-2024151 and AHUCM-rats-2024149).

Consent to participate

Not applicable to this article.

Consent to publish

Not applicable to this article.

Competing interests

The authors have no relevant financial or nonfinancial interests to disclose.

Funding

The authors acknowledge financial support from the National Natural Science Foundation of China (No. 82374301, 82574875), the State Key Laboratory of Southwestern Chinese Medicine Resources (No. SKLTCM202410), the Key Project of Anhui Province Department of Education (No. 2023AH030070, 2024AH051040), Anhui Province Key Laboratory, China (KFKT202305, 2024ZYFBAHKLA11, and 2024ZYFBAHKLA15), and Greater Health Research Institute of Hefei Comprehensive National Science Center, China (2023CXMMTCM005).

Author Contribution

Fan Li: Conceptualization, Data curation, Methodology, Writing - original draft. Haitao Zheng: Formal analysis, Investigation, Software. Weisheng Xu: Data curation, Validation, Visualization. Annan Jiao: Methodology, Investigation. Fan Yang: Validation, Methodology, Software. Haoyu Wu: Validation, Methodology, Software. Mengmeng Yang: Validation, Methodology, Software. Binqian Yao: Validation, Methodology, Software. Zhifa Zhu: Validation, Methodology, Software. Jiabing Tong: Validation, Methodology, Software. Dahai Zhao: Funding acquisition, Supervision. Nianzhi Zhang: Investigation, Writing - review & editing. Yang Chen: Project administration, Supervision, Writing - review & editing. Zhenbao Li: Conceptualization, Formal analysis, Supervision, Funding acquisition, Writing - review & editing.

Data Availability

The datasets generated during the current study are available from the corresponding author on reasonable request.

References

1. Kim SY, Park HS, Chiang AC. Small Cell Lung Cancer: A Review. JAMA. 2025. https://10.1001/jama.2025.0560.
2. Meyer ML, Fitzgerald BG, Paz-Ares L, Cappuzzo F, Janne PA, Peters S, Hirsch FR. New promises and challenges in the treatment of advanced non-small-cell lung cancer. Lancet (London England). 2024. https://10.1016/S0140-6736(24)01029-8.
3. The L. Lung cancer treatment: 20 years of progress. Lancet (London England). 2024. https://10.1016/S0140-6736(24)01299-6.
4. Caruso G, Weroha SJ, Cliby W. Ovarian Cancer: A Review. JAMA. 2025. https://10.1001/jama.2025.9495.
5. Megyesfalvi Z, Gay CM, Popper H, Pirker R, Ostoros G, Heeke S, Lang C, Hoetzenecker K, Schwendenwein A, Boettiger K, Bunn PA Jr., Renyi-Vamos F, Schelch K, Prosch H, Byers LA, Hirsch FR, Dome B. Clinical insights into small cell lung cancer: Tumor heterogeneity, diagnosis, therapy, and future directions. CA Cancer J Clin. 2023. https://10.3322/caac.21785.
6. Zhang Y, Zhang W, Wang Y, Zhu J, Zhou M, Peng C, He Z, Sun J, Li Z, Gui S. Emerging nanotaxanes for cancer therapy. Biomaterials. 2021. https://10.1016/j.biomaterials.2021.120790.
7. Zhang Y, Cui H, Zhang R, Zhang H, Huang W. Nanoparticulation of Prodrug into Medicines for Cancer Therapy. Adv Sci (Weinh). 2021. https://10.1002/advs.202101454.
8. Li Y, Sun Y, Yan Q, Wang W, Wang S, Wang Q, Wang D, Yuan J, Sun J, He Z, Li Z, Sun B. Redox-triggered prodrug nanoassemblies with high tumor selectivity and biocompatibility break through antitumor dilemma of paclitaxel. Chin Chem Lett. 2025. https://10.1016/j.cclet.2025.111350.
9. Li F, Wang W, Xu W, Li W, Lu Y, Wang R, He Z, Feng Z, Tong J, Li Z. Traditional Chinese medicine-facilitated redox-labile paclitaxel dimer nanoprodrug for efficient chemoimmunotherapy. J Pharm Anal. 2025. https://10.1016/j.jpha.2025.101348.
10. Guo T, Zhong H, Li X, Mu J, Liu T, Yu N, Zhao Y, Liang XJ, Guo S. Drug content on anticancer efficacy of self-assembling ketal-linked dextran-paclitaxel conjugates. J controlled release: official J Controlled Release Soc. 2023. https://10.1016/j.jconrel.2023.05.045.
11. Dong C, Zhou Q, Xiang J, Liu F, Zhou Z, Shen Y. Self-assembly of oxidation-responsive polyethylene glycol-paclitaxel prodrug for cancer chemotherapy. J controlled release: official J Controlled Release Soc. 2020. https://10.1016/j.jconrel.2020.02.038.
12. Du J, Zong L, Li M, Yu K, Qiao Y, Yuan Q, Pu X. Two-Pronged Anti-Tumor Therapy by a New Polymer-Paclitaxel Conjugate Micelle with an Anti-Multidrug Resistance Effect. Int J Nanomed. 2022. https://10.2147/IJN.S348598.
13. Hao D, Meng Q, Jiang B, Lu S, Xiang X, Pei Q, Yu H, Jing X, Xie Z. Hypoxia-Activated PEGylated Paclitaxel Prodrug Nanoparticles for Potentiated Chemotherapy. ACS Nano. 2022. https://10.1021/acsnano.2c05341.

14. Guo J, Zhang X, Dong F, Wang S, Wang D, Li Y, Zuo S, Wang Q, Li W, Sun J, He Z, Zhang T, Jiang Q, Sun B. Revealing the impact of modified modules flexibility on gemcitabine prodrug nanoassemblies for effective cancer therapy. J Colloid Interface Sci. 2025. https://10.1016/j.jcis.2024.08.026.
15. Zuo S, Liu T, Li L, Xu H, Guo J, Wang Q, Yang Y, He Z, Sun J, Sun B. Tetrasulfide bond boosts the anti-tumor efficacy of dimeric prodrug nanoassemblies. Cell Rep Med. 2024. https://10.1016/j.xcrm.2024.101432.
16. Zheng S, Li G, Fu S, Wang N, Qiao H, Li M, Zhang X, Wang K, Sun W, Tian C, He Z, Ouyang D, Sun B, Sun J. Hybrid nanoassembly indicating a synthetic lethality relationship induces mitotic catastrophe-mediated tumor elimination. Chem Eng J. 2024. https://10.1016/j.cej.2023.147802.
17. Liu T, Li L, Wang S, Dong F, Zuo S, Song J, Wang X, Lu Q, Wang H, Zhang H, Cheng M, Liu X, He Z, Sun B, Sun J. Hybrid chalcogen bonds in prodrug nanoassemblies provides dual redox-responsivity in the tumor microenvironment. Nat Commun. 2022. https://10.1038/s41467-022-35033-7.
18. Zhao D, Tao W, Li S, Chen Y, Sun Y, He Z, Sun B, Sun J. Apoptotic body-mediated intercellular delivery for enhanced drug penetration and whole tumor destruction. Sci Adv. 2021. https://10.1126/sciadv.abg0880.
19. Yu J, Zhong B, Zhao L, Hou Y, Ai N, Lu JJ, Ge W, Chen X. Fighting drug-resistant lung cancer by induction of NAD(P)H:quinone oxidoreductase 1 (NQO1)-mediated ferroptosis. Drug resistance updates: reviews and commentaries in antimicrobial and anticancer chemotherapy. 2023. https://10.1016/j.drup.2023.100977
20. Pei Q, Lu S, Zhou J, Jiang B, Li C, Xie Z, Jing X. Intracellular Enzyme-Responsive Profluorophore and Prodrug Nanoparticles for Tumor-Specific Imaging and Precise Chemotherapy. ACS Appl Mater Interfaces. 2021. https://10.1021/acsami.1c19058.
21. Liu P, Huang Y, Zhan C, Zhang F, Deng C, Jia Y, Wan T, Wang S, Li B. Tumor-overexpressed enzyme responsive amphiphiles small molecular self-assembly nano-prodrug for the chemo-phototherapy against non-small-cell lung cancer. Mater Today Bio. 2023. https://10.1016/j.mtbio.2023.100722.
22. Xi Z, Dai R, Ze Y, Jiang X, Liu M, Xu H. Traditional Chinese medicine in lung cancer treatment. Mol Cancer. 2025. https://10.1186/s12943-025-02245-6.
23. He L, Edi S, Ma J, Kong Z, Dai C, Huang L, Zeng R, Gou K. Prevention and treatment of radiation injury by traditional Chinese medicine: A review. Chin Herb Med. 2025. https://10.1016/j.chmed.2024.09.005.
24. Liu Y, Li X, Chen C, Ding N, Ma S, Yang M. Exploration of compatibility rules and discovery of active ingredients in TCM formulas by network pharmacology. Chin Herb Med. 2024. https://10.1016/j.chmed.2023.09.008.
25. Tong JB, Zhang XX, Wang XH, Zeng SJ, Wang DY, Zhang ZQ, Hu J, Yang C, Li ZG. Qiyusanlong decoction suppresses lung cancer in mice via Wnt/beta-catenin pathway. Mol Med Rep. 2018. https://10.3892/mmr.2018.8478.
26. Yu W, Hua Y, Qiu H, Hao J, Zou K, Li Z, Hu S, Guo P, Chen M, Sui S, Xiong Y, Li F, Lu J, Guo W, Luo G, Deng W. PD-L1 promotes tumor growth and progression by activating WIP and beta-catenin

signaling pathways and predicts poor prognosis in lung cancer. Cell Death Dis. 2020. https://10.1038/s41419-020-2701-z.

27. Cha JH, Chan LC, Li CW, Hsu JL, Hung MC. Mechanisms Controlling PD-L1 Expression in Cancer. Mol Cell. 2019. https://10.1016/j.molcel.2019.09.030.
28. Soltani M, Abbaszadeh M, Fouladseresht H, Sullman MJM, Eskandari N. PD-L1 importance in malignancies comprehensive insights into the role of PD-L1 in malignancies: from molecular mechanisms to therapeutic opportunities. Clin Exp Med. 2025. https://10.1007/s10238-025-01641-y.
29. Shen S, Hong Y, Huang J, Qu X, Sooranna SR, Lu S, Li T, Niu B. Targeting PD-1/PD-L1 in tumor immunotherapy: Mechanisms and interactions with host growth regulatory pathways. Cytokine Growth Factor Rev. 2024. https://10.1016/j.cytogfr.2024.08.001.

Scheme. 1

Schemes 1 is available in the Supplementary Files section.

Figures

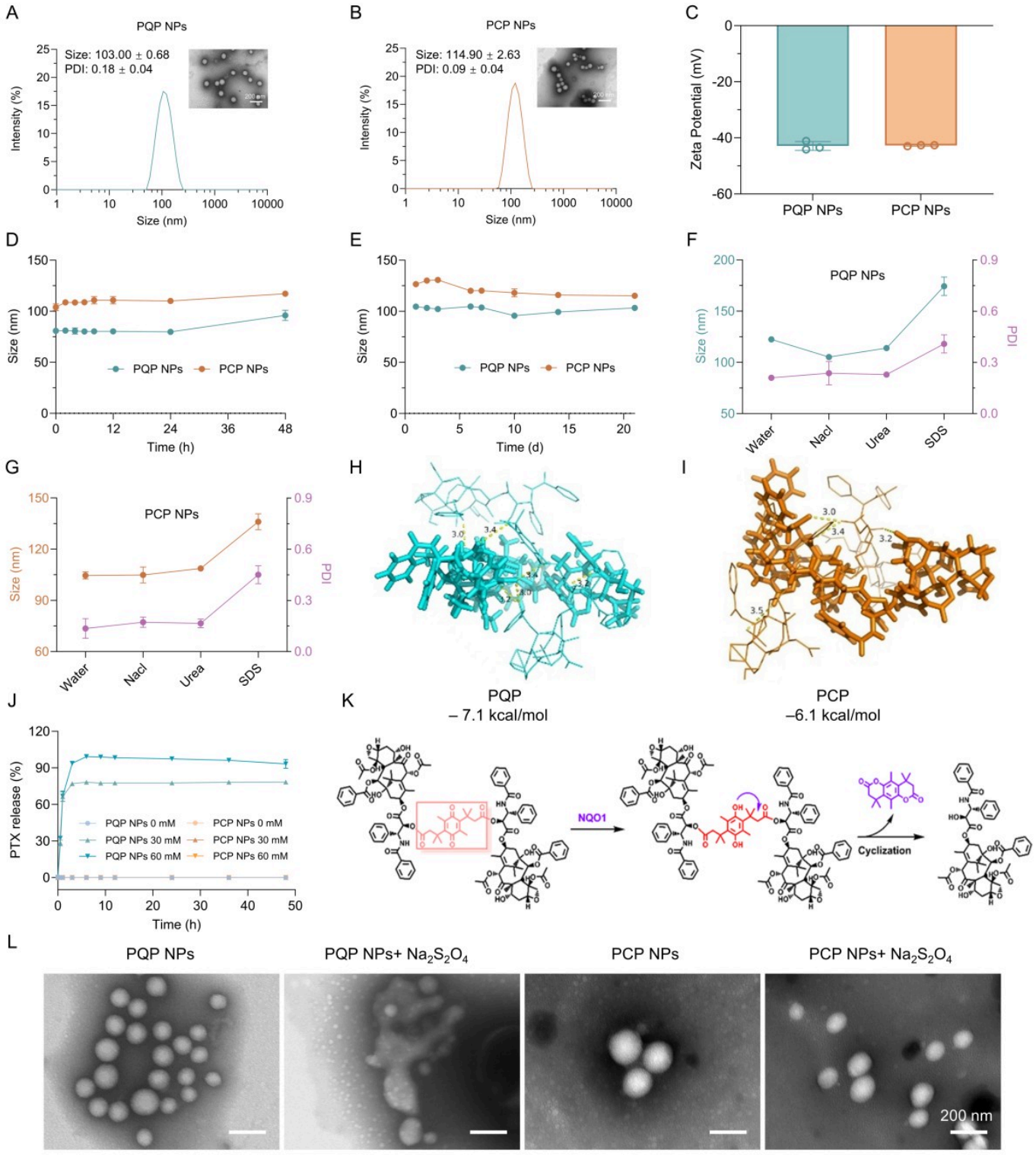


Figure 1

Characterization and PTX release of full-active NPs. Hydrodynamic diameter and TEM image of PQP NPs (**A**) and PCP NPs (**B**). Z**eta** potentials (**C**) of PQP NPs and PCP NPs. Particle size changes of PQP NPs and PCP NPs incubated with PBS (pH 7.4) containing 10% FBS (**D**) and deionized water (**E**) for different times. The changes of particle size and PDI of PQP NPs (**F**) and PCP NPs (**G**) incubated in Water, NaCl, Urea, and SDS for 24 h. Molecular docking and binding energy of PQP (**H**) and PCP (**I**).

NQO1-responsive PTX release (**J**) of PQP NPs and PCP NPs in release media containing 30 mM and 60 mM $Na_2S_2O_4$. The release mechanism of PQP NPs (**K**) triggered by $Na_2S_2O_4$. TEM images (**L**) of PQP NPs and PCP NPs treated with or without 60 mM $Na_2S_2O_4$ for 12 h. Data are expressed as mean ± SD (*n* = 3).

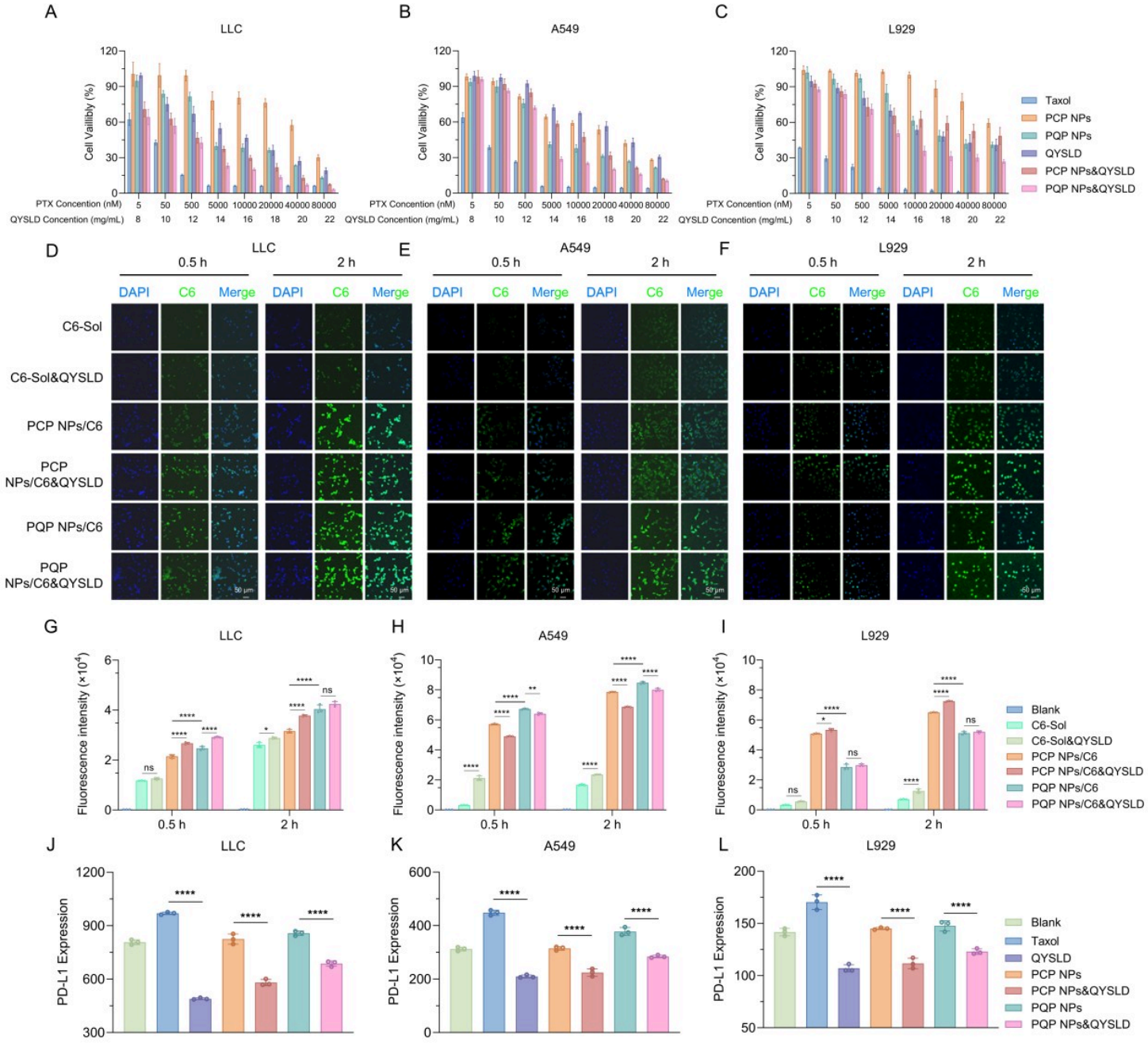


Figure 2

Cytotoxicity, cellular uptake and PD-L1 expression. Viability of LLC (**A**), A549 (**B**), and L929 cells (**C**) incubated with Taxol, PQP NPs, PCP NPs, QYSLD, PQP NPs&QYSLD, and PCP NPs&QYSLD for 48 h assessed by CCK-8 assay. The mean fluorescence intensity of LLC (**D**), A549 (**E**), and L929 cells (**F**) incubated with C6-Sol, C6-Sol&QYSLD, PQP NPs/C6, PCP NPs/C6, PQP NPs/C6&QYSLD, and PCP

NPs/C6&QYSLD analyzed by FCM. CLSM images of LLC (**G**), A549 (**H**), and L929 cells (**I**) cultured with C6-Sol, C6-Sol&QYSLD, PQP NPs/C6, PCP NPs/C6, PQP NPs/C6&QYSLD, and PCP NPs/C6&QYSLD for 0.5 h and 2 h, respectively. PD-L1 expression levels in LLC (**J**), A549 (**K**), and L929 cells (**L**) incubated with Taxol, QYSLD, PQP NPs, PCP NPs, PQP NPs&QYSLD, and PCP NPs&QYSLD for 12 h at twice the IC_{50} concentration of PTX analyzed by FCM. Data are expressed as mean ± SD ($n \geq 3$). *p< 0.05, **p < 0.01, ****p < 0.0001; ns, not significant.

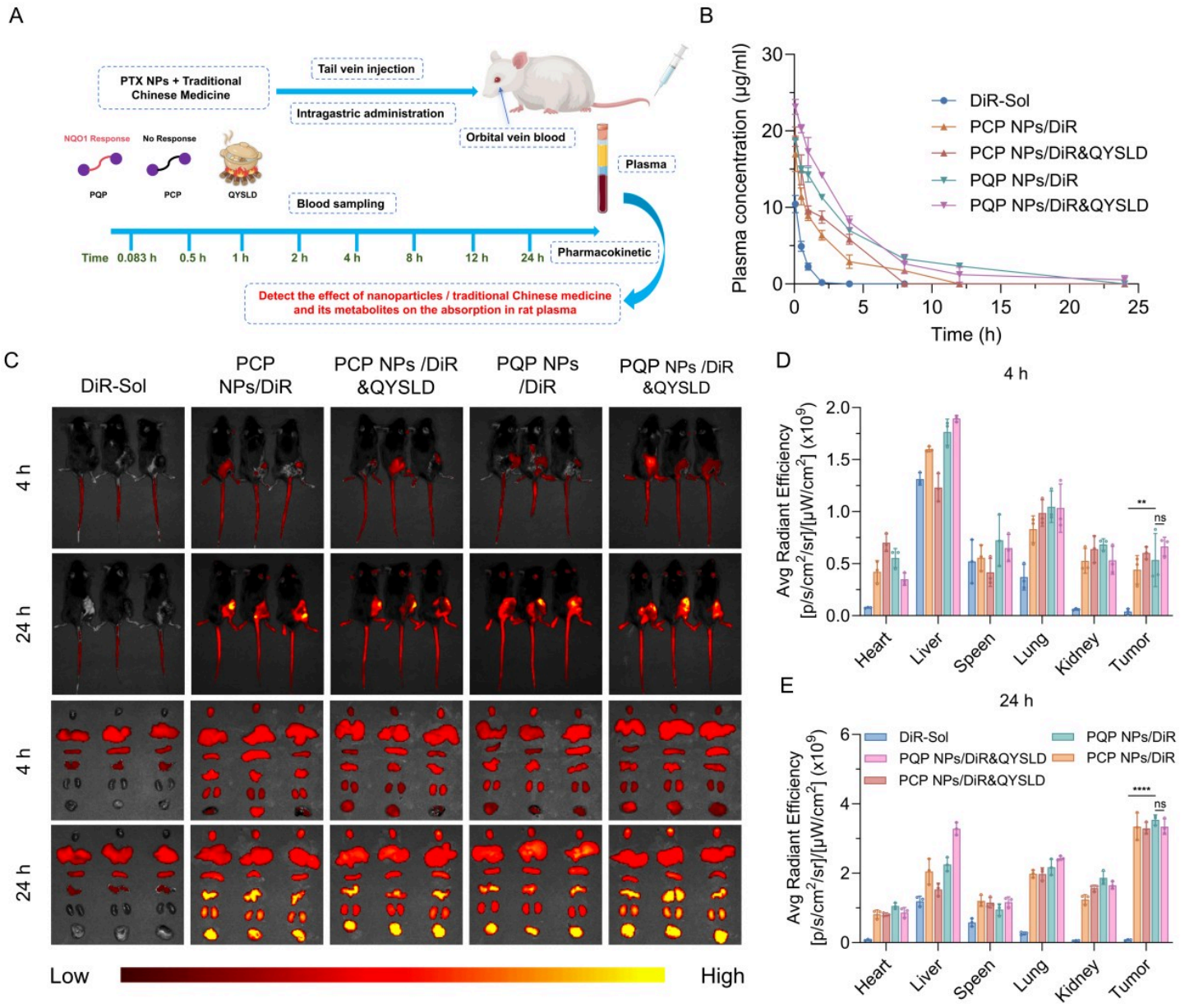


Figure 3

Pharmacokinetics and biodistribution of QYSLD in combination with full-active NPs. (**A**) Schematic of the pharmacokinetic study and (**B**) the corresponding plasma concentration profiles of DiR-Sol and DiR-labeled NPs. (**C**) *In vivo*fluorescence images and *ex vivo* fluorescence distribution in isolated tissues (heart, liver, spleen, lungs, kidneys, and tumor) from LLC tumor-bearing mice at 4 h and 24 h post-

injection of DiR-Sol and DiR-labeled NPs. Quantitative analysis of the fluorescence intensity in the isolated organs at (**D**) 4 h and (**E**) 24 h. Data are expressed as mean ± SD (n = 3). **p < 0.01, ****p < 0.0001; ns, not significant.

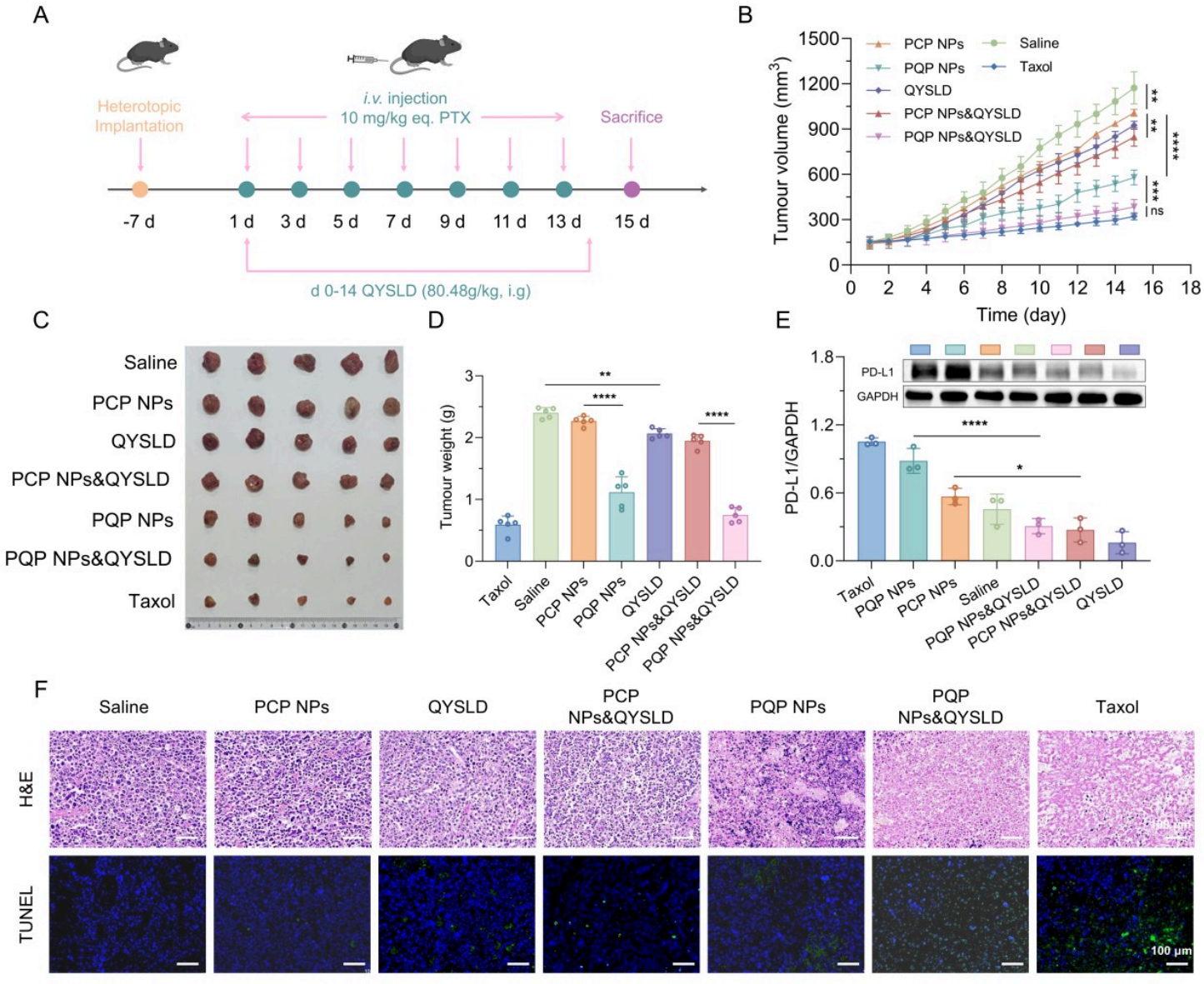


Figure 4

Antitumor efficacy of QYSLD in combination with full-active NPs in LLC tumor-bearing mice. (**A**) Schematic of the therapeutic treatment protocol. (**B**) Average relative tumor volume curves. (**C**) Representative photographs of excised tumors. (**D**) Weights of excised tumors. (**E**) PD-L1 expression of LLC tumor tissues by Western blotting. (**F**) H&E and TUNEL staining images of isolated tumor sections in different groups. Scale bar: 100 μm. Data are expressed as mean ± SD (n ≥ 3). *p< 0.05, **p < 0.01, ***p < 0.001, ****p < 0.0001; ns, not significant.

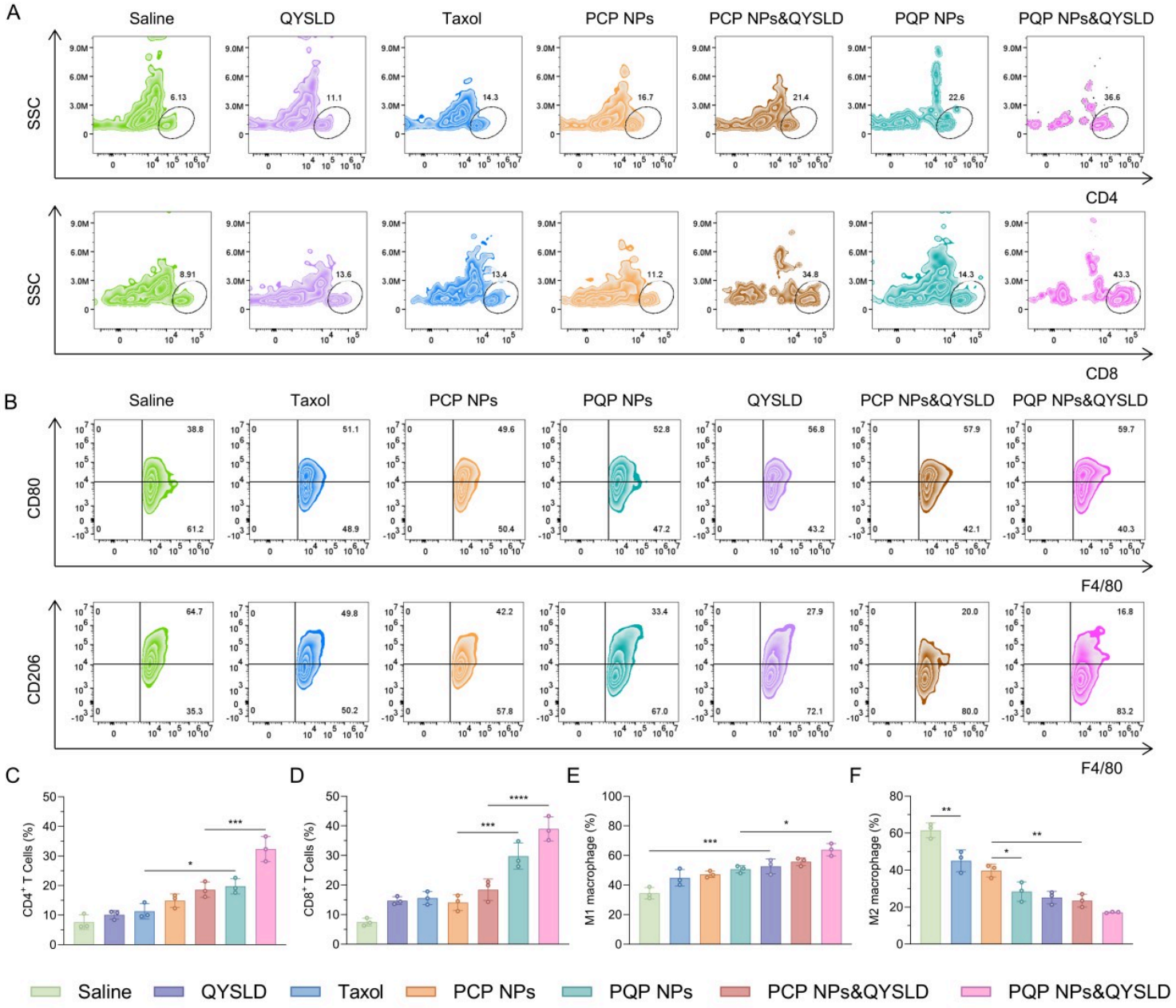


Figure 5

In vivo antitumor immune response of QYSLD in combination with full-active NPs. Quantitative analysis of $CD4^+$ T cells, $CD8^+$ T cells, M1 macrophages, and M2 macrophages in tumor tissues using FCM. Data are expressed as mean ± SD (n = 3). *p < 0.05, **p < 0.01, ***p < 0.001, ****p < 0.0001.

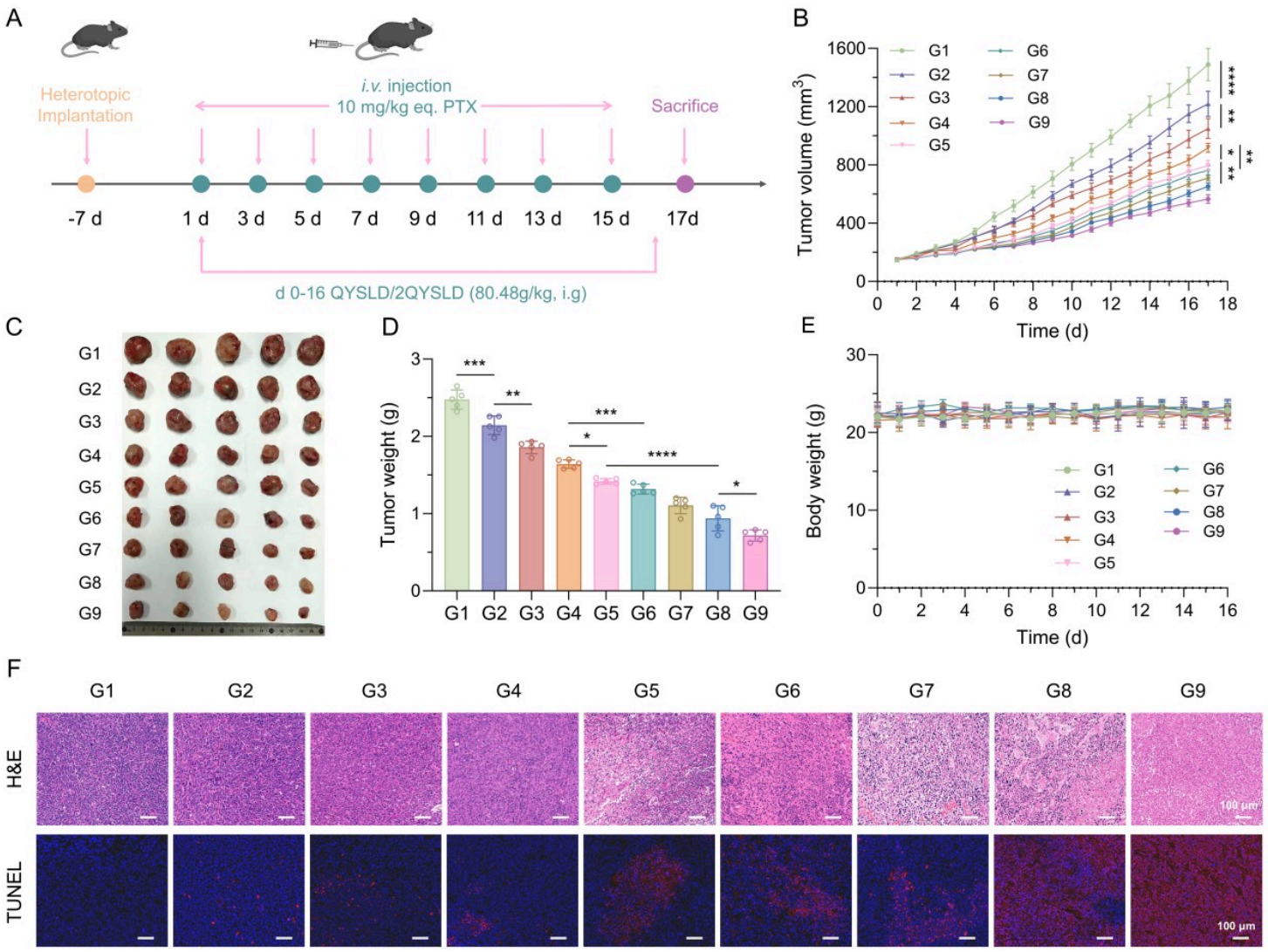


Figure 6

Antitumor efficacy of QYSLD in combination with commercially available nanomedicines in LLC tumor-bearing mice. (**A**) Schematic of the therapeutic treatment protocol. (**B**) Average relative tumor volume curves. (**C**) Representative photographs of excised tumors. (**D**) Weights of excised tumors. (**E**) Body weight changes of treated mice. (**F**) H&E and TUNEL staining images of isolated tumor sections in different groups. Scale bar: 100 μm. Data are expressed as mean ± SD (n = 5). *p < 0.05, **p< 0.01, ***p < 0.001, ****p < 0.0001. (G1: Saline, G2: QYSLD, G3: 2QYSLD, G4: Lipusu, G5: Abraxane, G6: Lipusu&QYSLD, G7: Lipusu&2QYSLD, G8: Abraxane&QYSLD, G9: Abraxane&2QYSLD).

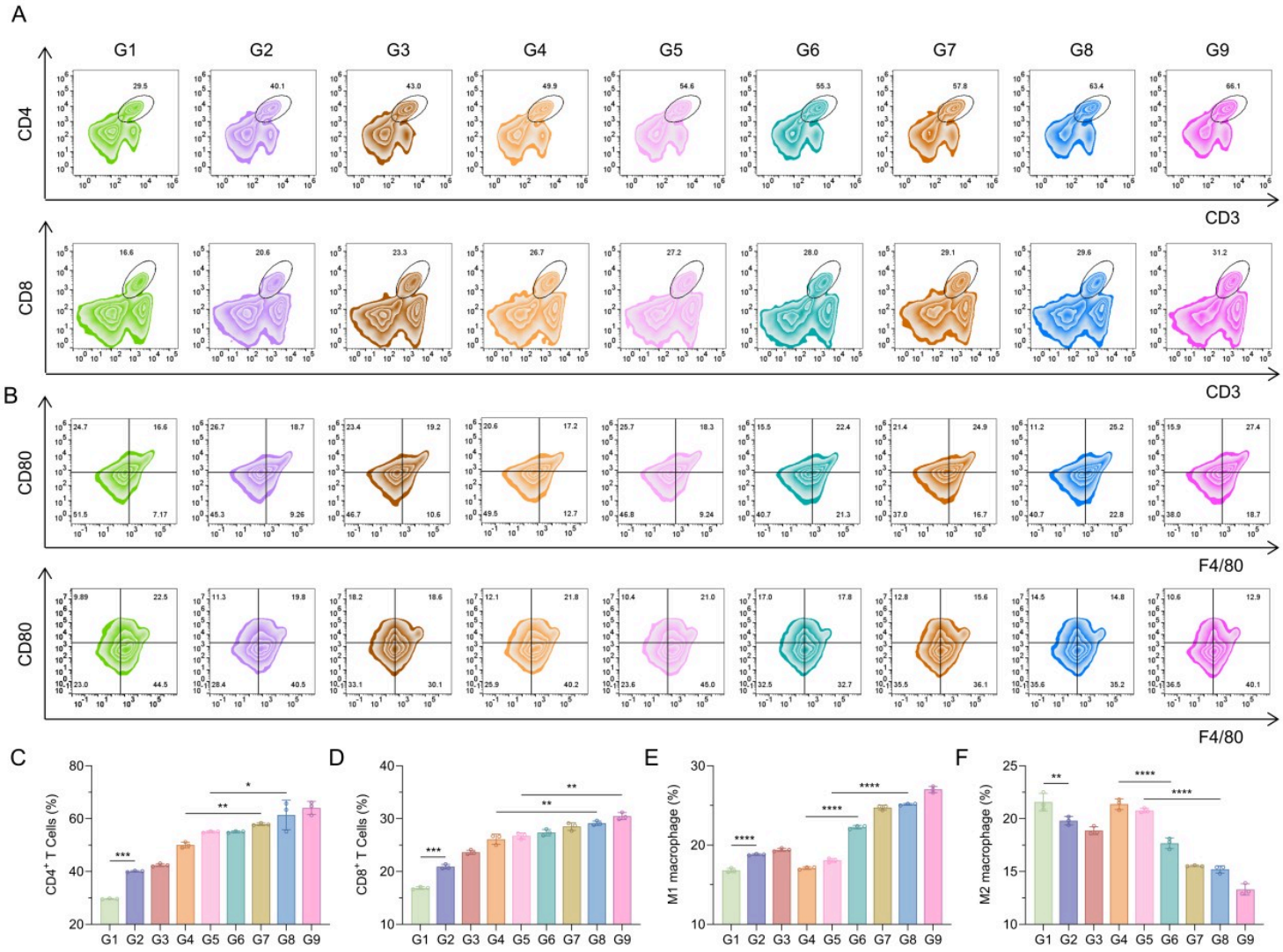


Figure 7

In vivo antitumor immune response of QYSLD in combination with commercially available nanomedicines. FCM analysis of $CD4^+$ T cells, $CD8^+$ T cells, M1 macrophages, and M2 macrophages in tumor tissues. Data are expressed as mean ± SD (n = 3). *p< 0.05, **p < 0.01, ***p < 0.001, ****p < 0.0001. (G1: Saline, G2: QYSLD, G3: 2QYSLD, G4: Lipusu, G5: Abraxane, G6: Lipusu&QYSLD, G7: Lipusu&2QYSLD, G8: Abraxane&QYSLD, G9: Abraxane&2QYSLD).

Supplementary Files

This is a list of supplementary files associated with this preprint. Click to download.

- Supportinginformation.docx
- Scheme.png